

Coherent phonon dynamics in spatially separated graphene mechanical resonators

Zhuo-Zhi Zhang^{a,b,1}, Xiang-Xiang Song^{a,b,1,2}, Gang Luo^{a,b,1}, Zi-Jia Su^{a,b}, Kai-Long Wang^{a,b}, Gang Cao^{a,b}, Hai-Ou Li^{a,b}, Ming Xiao^{a,b}, Guang-Can Guo^{a,b}, Lin Tian^{c,2}, Guang-Wei Deng^{a,b,2}, and Guo-Ping Guo^{a,b,d,2}

^aChinese Academy of Sciences Key Laboratory of Quantum Information, University of Science and Technology of China, 230026 Hefei, Anhui, China; bChinese Academy of Sciences Center for Excellence in Quantum Information and Quantum Physics, University of Science and Technology of China, 230026 Hefei, Anhui, China; Cschool of Nature Sciences, University of California, Merced, CA 95343; and Quantum Chip Lab, Origin Quantum Computing Company Limited, 230088 Hefei, Anhui, China

Edited by Paul L. McEuen, Cornell University, Ithaca, NY, and approved February 6, 2020 (received for review September 30, 2019)

Vibrational modes in mechanical resonators provide a promising candidate to interface and manipulate classical and quantum information. The observation of coherent dynamics between distant mechanical resonators can be a key step toward scalable phononbased applications. Here we report tunable coherent phonon dynamics with an architecture comprising three graphene mechanical resonators coupled in series, where all resonators can be manipulated by electrical signals on control gates. We demonstrate coherent Rabi oscillations between spatially separated resonators indirectly coupled via an intermediate resonator serving as a phonon cavity. The Rabi frequency fits well with the microwave burst power on the control gate. We also observe Ramsey interference, where the oscillation frequency corresponds to the indirect coupling strength between these resonators. Such coherent processes indicate that information encoded in vibrational modes can be transferred and stored between spatially separated resonators, which can open the venue of on-demand phonon-based information processing.

graphene mechanical resonator | phonon-based information processing | coherent oscillation

ver the past decade, one of the major achievements in Over the past decade, one of the image nanotechnology was the realization of phonon-state storage and transfer (1-9). Scalable phonon-based classical (10) and quantum (6, 7) information processing requires manipulation of highly coherent phonon modes with tunable coupling. Efforts toward phonon-state manipulation have been made in different systems, such as the dynamical control of phonon states between different modes in a single mechanical resonator (10-12) or between modes in neighboring mechanical resonators (13), the observation of static phonon states of spatially separated mechanical resonators with indirect coupling (14), and routing of microwave phonons using phonon waveguide (15). Theoretical works also proposed that couplings between two spatially separated mechanical oscillators via the exchange of virtual photon pairs can be achieved (16). However, observation of tunable coherent dynamics of indirectly coupled phonon modes remains a challenge, due to the requirement on the combination of strong coupling, long coherence time, and tunability of phonon modes.

Graphene-based mechanical resonators with high-quality factors and excellent electrical control provides us with a promising platform for tunable phonon manipulations (17-21). Here we use highquality graphene-based mechanical resonators to demonstrate coherent phonon dynamics. We report the observation of coherent Rabi and Ramsey oscillations (22, 23) between spatially separated mechanical resonators in the classical regime via Raman-like indirect coupling (14). Our results indicate that phonon coherence can be maintained and controlled over distant resonators, which will shed light on scalable phonon-based information processing.

Sample Characterization. As shown in Fig. 1 A and B, a graphene ribbon with a width of \sim 2.2 µm and \sim 7 layers is suspended over three trenches (2 µm in width, 200 nm in depth) between four contact electrodes. This structure defines three electromechanical resonators, labeled as R_1 , R_2 , and R_3 in Fig. 1A, respectively. All measurements were carried out in a dilution refrigerator at a base temperature of ~ 10 mK and a pressure below 10^{-7} Torr. Similar structure was used to realize indirect coupling between mechanical resonators via a Raman-like process with static presentations (14). Here optimizing the measurements setup and the quality of the device allows us to employ this system to explore tunable coherent phonon dynamics in spatially separated mechanical resonators.

We characterize each resonator separately using the onesource frequency-modulation technique (24), where a frequencymodulated (FM) signal, $V^{\text{FM}}(t) = V^{\text{AC}} \cos \left[2\pi f_{\text{d}}t + \frac{f_{\Delta}}{f_{\text{L}}} \sin(2\pi f_{\text{L}}t) \right]$, is applied at a selected contact, and the mixing current I_{mix} at frequency f_L is recorded by a lock-in amplifier at another contact, as illustrated in Fig. 1B. We find that the relaxation rate of the resonators shows strong dependency on the driving amplitude.

Significance

The rapid development of nanotechnologies enables the possibility to use long-lifetime vibrational phonon modes for classical and quantum information processing. Despite continuous efforts in the past decade, tunable phonon-mediated transferring and processing of information between distant phonon modes remains technically challenging. Taking advantage of the excellent electronic and mechanical properties of graphene, we are able to realize electrically tunable coherent phonon dynamics between spatially separated graphene mechanical resonators. The gate-controllable resonant frequencies, coupling strengths, and coherent phonon dynamics indicate that information encoded in vibrational modes can be stored, transferred, and manipulated between spatially separated resonators. Our results not only demonstrate the transfer of information between phonons, but also provide the building blocks toward scalable phonon-based information processing.

Author contributions: X.-X.S., G.-W.D., and G.-P.G. designed research; Z.-Z.Z., X.-X.S., G.L., K.-L.W., G.C., H.-O.L., M.X., G.-C.G., and G.-W.D. performed research; Z.-Z.Z., X.-X.S., Z.-J.S., L.T., and G.-W.D. analyzed data; and Z.-Z.Z., X.-X.S., G.L., Z.-J.S., K.-L.W., G.C., H.-O.L., M.X., G.-C.G., L.T., G.-W.D., and G.-P.G. wrote the paper.

The authors declare no competing interest

This article is a PNAS Direct Submission.

Published under the PNAS license.

Data deposition: Raw data corresponding to the findings of this study have been deposited at Zenodo, https://zenodo.org/record/3594242#.XkXLamhKhPY.

¹Z.-Z.Z., X.-X.S., and G.L. contributed equally to this work.

²To whom correspondence may be addressed. Email: songxx90@ustc.edu.cn, Itian@ ucmerced.edu, gwdeng@ustc.edu.cn, or gpguo@ustc.edu.cn.

This article contains supporting information online at https://www.pnas.org/lookup/suppl/ doi:10.1073/pnas.1916978117/-/DCSupplemental.

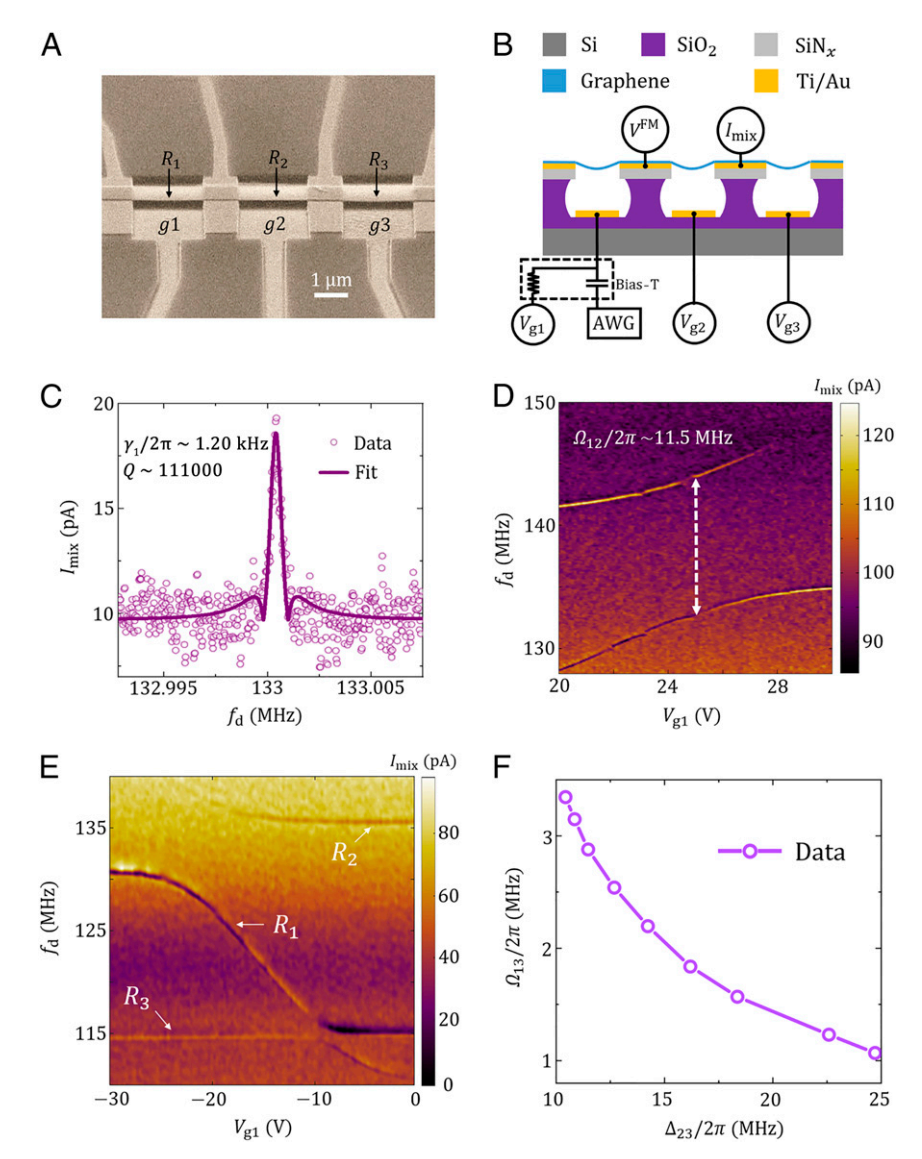


Fig. 1. Sample structure and mode spectra of the resonators. (*A*) Scanning electron microscope image of a typical sample with a tilted view angle. Four contacts divide a suspended graphene ribbon into three mechanical resonators, R_1 , R_2 , and R_3 , in a linear chain. (*B*) Schematic sample structure and measurement setup. A frequency-modulated microwave signal V^{FM} is applied through one contact of the center resonator, and a lock-in amplifier detects the mixing current I_{mix} at the modulation frequency of the inputted FM signal at another contact. The frequencies of the resonators are tuned by dc voltages on the gates, respectively. An arbitrary waveform generator (AWG) is connected to gate g1 to provide additional burst signals for the coherent oscillations. (C) The mixing current as a function of the driving frequency f_0 at $V_{g1} = 22$ V. The measured linewidth of resonator R_1 is $γ_1/2π \sim 1.20$ kHz. Similarly, the linewidth of R_2 is $γ_2/2π \sim 1.16$ kHz and the linewidth of R_3 is $γ_3/2π \sim 0.73$ kHz (*Sl Appendix*, Fig. S2) at a driving power of ~ 60 dBm. (*D*) The mixing-current spectrum of resonators R_1 and R_2 . Coupling strength as large as 11.5 MHz is observed. Here $V_{g2} = 17$ V and $V_{g3} = 0$ V. (*E*) Spectrum of all three resonators. Here R_2 is far off-resonance from R_3 with a detuning $\Delta_{23}/2π \sim 20$ MHz, with $\Delta_{23} = 10$ V. The dc voltage $\Delta_{23} = 10$ V. The dc voltage $\Delta_{23} = 10$ V. The measured indirect coupling is observed when $\Delta_{23} = 10$ D and $\Delta_{23} = 10$ D a

At a low driving amplitude, \sim -60 dBm, we extract the relaxation rate to be $\gamma_1/2\pi=1.20$ kHz from the spectrum of the mixing current $I_{\rm mix}$ by fitting (24), as shown in Fig. 1C and SI Appendix, Fig. S2, which corresponds to a quality factor of $Q_1=f_{\rm m1}/\gamma_1\times 2\pi$ \sim 111,000 for resonator R_1 . Comparing to our previous work (14), observed quality factor is increased mainly due to that frequency-modulation technique allows for lower probing power (25). At a stronger driving power of \sim -45 dBm, the relaxation rate becomes $\gamma_1/2\pi \sim 300$ kHz, corresponding to a much lower quality factor of \sim 300. The relaxation rate increases significantly with increasing driving power due to nonlinear damping, which is similar to previous reports in nanomechanical systems (26, 27).

Note that we cannot estimate the magnitude of frequency fluctuations (28) and eliminate its influence in the present situation; what we obtained here is an upper bound of the relaxation rate. Here the resonant frequencies of all three resonators ($f_{\rm mi}$, i = 1, 2, and 3) can be tuned by adjusting the corresponding gate voltages $V_{\rm gi}$ (i = 1, 2, 3). Details of the characterization of the resonators can be found in *SI Appendix*, Figs. S1 and S2.

Strongly Coupled Mechanical Resonators. To characterize the coupling between the resonators R_1 and R_2 , we fix the frequency $f_{\rm m2}$ of R_2 (i.e., fix the gate voltage on gate g2) and tune $f_{\rm m1}$ by adjusting $V_{\rm g1}$. When $f_{\rm m1}$ approaches $f_{\rm m2}$, an avoided level crossing appears

in Fig. 1D. By measuring the frequency splitting, the coupling strength between neighboring resonators was obtained with $\Omega_{12}/2\pi \sim 11.5$ MHz. Here the coupling between the neighboring resonators R_1 and R_2 leads to a normal mode that is spatially distributed over the range of R_1 and R_2 . Similarly, we can measure the coupling strength between the neighboring resonators R_2 and R_3 , $\Omega_{23}/2\pi$, to be ~9.0 MHz, as shown in SI Appendix, Fig. S3. Since both R_1 and R_3 are neighboring to R_2 , avoided level crossing between R_1 and R_3 mediated by R_2 is observed, which can be translated to an effective coupling between the nonneighboring resonators (R_1 and R_3). The indirect coupling strength $\Omega_{13}/2\pi$ between the spatially separated resonators R_1 and R_3 is shown in Fig. 1E. The Raman-like effective coupling (14) $\Omega_{13}/2\pi$ decreases when the detuning Δ_{23} between f_{m2} and f_{m3} increases, as shown in Fig. 1F. With $\Omega_{13} \gg \gamma_1, \gamma_3$, the system is well in the strongcoupling regime.

Cooperativity is a key parameter to characterize the coherence and the potential for coherent manipulation of coupled modes. At low driving power \sim -60 dBm, we can calculate the zero-temperature cooperativities with $C_{12} = \Omega_{12}^2/\gamma_1\gamma_2$ for resonators R_1 and R_2 reaching 9.5×10^7 and $C_{23} = \Omega_{23}^2/\gamma_2\gamma_3$ for resonators R_2 and R_3 reaching 9.6×10^7 (see *SI Appendix*, Fig. S3 for details). More importantly, with effective coupling strength, $\Omega_{13}/2\pi \sim 3.3$ MHz, between the nonneighboring resonators R_1 and R_3 , the zero-temperature cooperativity $C_{13} = \Omega_{13}^2/\gamma_1\gamma_3$ between these spatially separated modes exceeds 1.2×10^7 , as shown in *SI Appendix*, Figs. S4 and S5. Such giant cooperativity is several orders of magnitude larger than previously reported results in coupled-mechanical systems (10, 11, 13, 14, 18, 19, 29–31), while for large driving power (\sim -45 dBm), where we conduct measurement on the coherent oscillations (Figs. 2 and 3), the increased relaxation

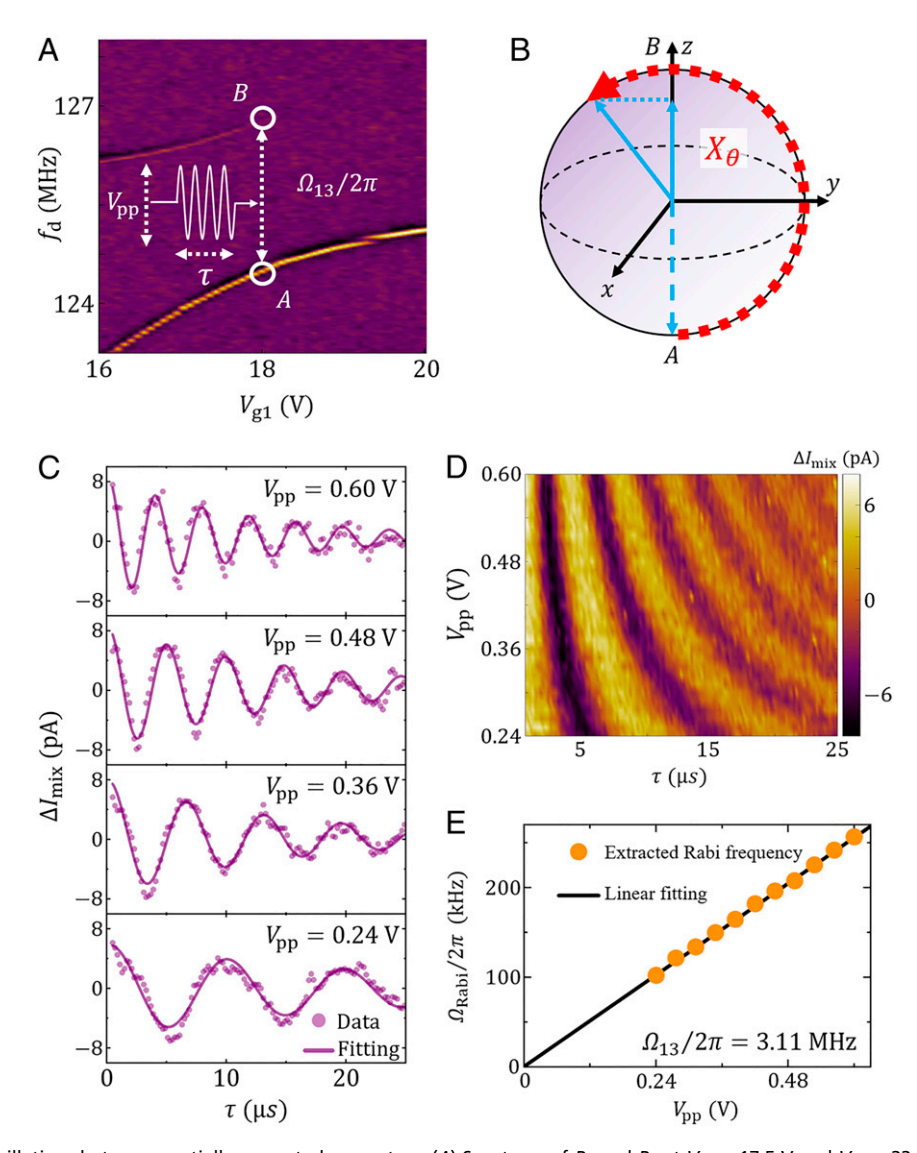


Fig. 2. Phonon Rabi oscillations between spatially separated resonators. (A) Spectrum of R_1 and R_3 at $V_{g2}=17.5$ V and $V_{g3}=22$ V with effective coupling strength $\Omega_{13}/2\pi=3.11$ MHz. During the experiment, we first excite the coupled system to eigenmode A, then apply a microwave burst to generate rotations around the x axis, and measure the mixing current at the frequency of eigenmode A. Each sequence is repeated for over 10^5 times to gather the data for the average mixing current. (B) Evolution of the system on the Bloch sphere. The dashed blue arrow marks the initial state. Under the microwave burst, the system rotates around the x axis, following the red trajectory, and the burst duration τ determines the rotation angle. (C) Average mixing current as a function of burst duration with microwave amplitudes $V_{pp}=0.60$, 0.48, 0.36, and 0.24 V, respectively. The purple lines show the damped cosinusoidal fits to the experimental data. (D) The Rabi oscillation versus the microwave amplitude V_{pp} . (E) Extracted Rabi frequency $\Omega_{Rabi}/2\pi$ as a function of microwave amplitude in comparison with a linear fitting (black line).

Zhang et al. PNAS Latest Articles | 3 of 6

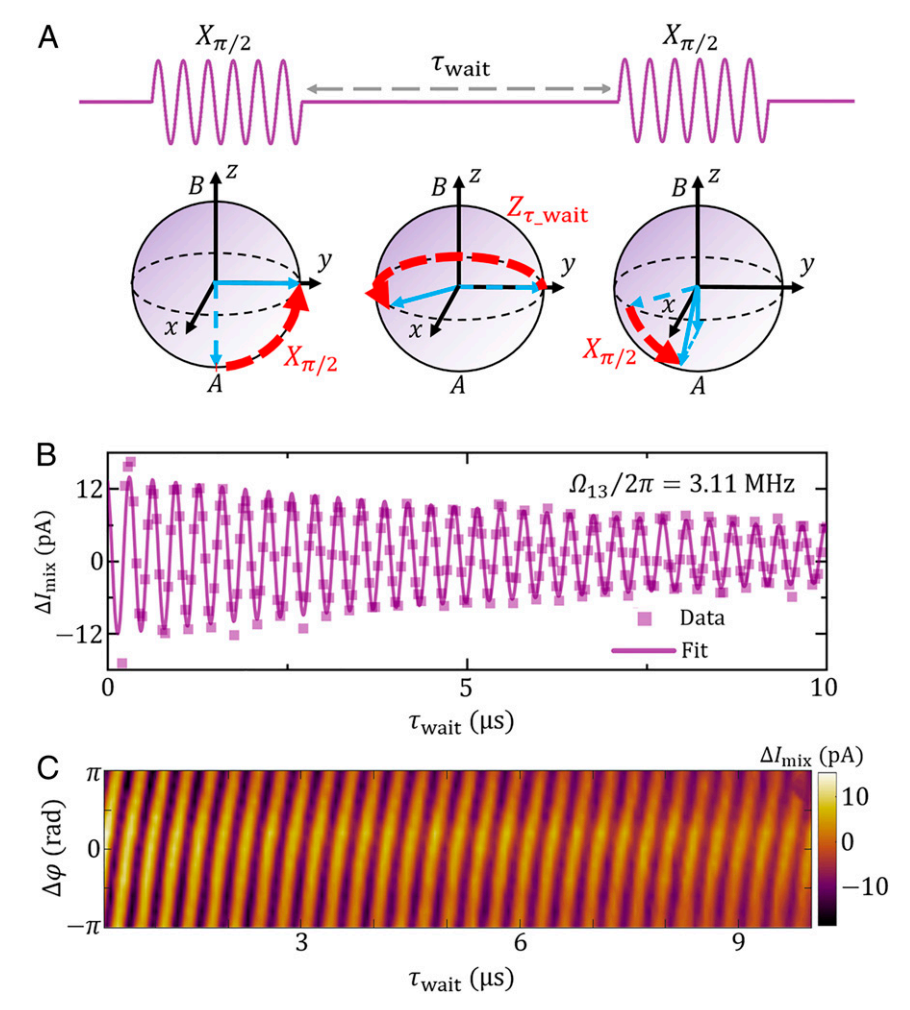


Fig. 3. Phonon Ramsey interference between spatially separated resonators. (A) Pulse sequence and system evolution in the Bloch sphere during Ramsey interference experiment. The pulse sequence consists of a $\pi/2$ rotation around the x axis, a free evolution duration τ_{wait} , and a second pulse around the x axis (or a selected axis in the x-y plane). The dashed blue arrows indicate the initial state of this system. The dashed red arrows indicate the evolution trajectories. The solid blue arrows refer to the final state. (B) Average mixing current as a function of τ_{wait} with coupling strength $\Omega_{13}/2\pi = 3.11$ MHz. The solid line is the numerical fitting using a damped cosinusoidal function, which gives an oscillation frequency $\Omega_{Ramsey}/2\pi = 3.12$ MHz, in good agreement with the coupling strength. (C) Ramsey interferences versus waiting time and relative phase $\Delta \varphi$ between the two $\pi/2$ pulses.

rate (~300 kHz) leads to zero-temperature cooperativities of C_{12} , $C_{23} \sim 1,000$, and $C_{13} \sim 100$. As mentioned above, the measured relaxation rate includes the effect of frequency fluctuations, which indicates that the actual cooperativity can be much larger. It is worthy to note that when considering thermal occupation [with average thermal phonon number $\bar{n}_{th} = 1/(e^{\hbar\omega/k_BT}-1) \sim 1.61$, where k_B is Boltzmann constant, T is around 10 mK], the finite-temperature cooperativity $C_{13}^{th} = C_{13}/\bar{n}_1^{th}\bar{n}_3^{th}$ is still sufficiently high for observing coherent phonon dynamics shown in Figs. 2 and 3.

Rabi Oscillations between Spatially Separated Resonators. The high cooperativity between resonators R_1 and R_3 is the basis for high-fidelity state transfer within these spatially separated modes. To demonstrate this, we perform time-domain experiments to study such coherent oscillations. First, we bias the system at $V_{\rm g1}=18~\rm V$, $V_{\rm g2}=17.5~\rm V$, and $V_{\rm g3}=22~\rm V$. At this condition, the resonators R_1 and R_3 are degenerate, as indicated by the anticrossing between these modes. We initialize the coupled system to be excited at the lower eigenmode, which is labeled as A in Fig. 2A, with A being the symmetric superposition of R_1 and R_3 . We then apply a microwave burst at the frequency $f_{\rm MW}=\Omega_{13}/2\pi=3.11~\rm MHz$ on gate g_1 . The measured mixing current demonstrates Rabi oscillations

between the lower eigenmode A and the upper eigenmode B, as a function of the duration of the burst. In analogy to a two-level system, the dynamics of the phonon excitation can be illustrated with the Bloch sphere of theses eigenmodes (Fig. 2B), where eigenmode A is the south pole of the sphere, and eigenmode B is the north pole (10, 23). Under the microwave burst, the system rotates around the x axis of the Bloch sphere and exhibits a Rabi oscillation. The population of eigenmode A oscillates with the duration τ of the burst, which generates coherent oscillation in the mixing current I_{mix} detected at the frequency of the eigenmode A. The mixing current versus the microwave duration τ at different pulse amplitude $V_{\rm pp}$ (peak to peak) is plotted in Fig. 2 C and D. The time dependence of I_{mix} can be fitted with a damped cosinusoidal function, $Ae^{-\tau/T_{\text{Rabi}}}\cos(\Omega_{\text{Rabi}}\tau)$, with damping time $T_{\rm Rabi}$ and Rabi frequency $\Omega_{\rm Rabi}/2\pi$. In the upper panel of Fig. 2C, the Rabi frequency is ~ 0.25 MHz with damping time $T_{\text{Rabi}} \sim 11.6$ μ s, with burst amplitude $V_{pp} = 0.60$ V. In Fig. 2E, the measured Rabi frequency is plotted versus the voltage amplitude V_{pp} and shows a linear dependence on the amplitude, in agreement with our analysis (32). Details of eigenmodes A and B and their dynamics are presented in SI Appendix, section S7.

Ramsey Interference between Spatially Separated Resonators. Next, we study the precession dynamics between resonators R_1 and R_3 in a Ramsey interference experiment. The phonon excitation is initially prepared in eigenmode A, similar to that of the Rabi oscillation experiment. In the beginning of each cycle, a $\pi/2$ pulse ($V_{pp} = 0.60 \text{ V}$ and pulse duration ~1.1 µs) along the x axis is applied to this system, which rotates the state to the x-y plane in the Bloch sphere. This system then undergoes a free evolution of duration τ_{wait} . During the free evolution, the system rotates around the z axis governed by $\Omega_{13}/2\pi$. A second $\pi/2$ pulse in the x axis is then applied to rotate the state. This process is illustrated in Fig. 34. We measure the mixing current at the frequency of eigenmode A. The average mixing current versus τ_{wait} is shown in Fig. 3B, together with a damped cosinusoidal function $Ae^{-\tau/T_{\text{Ramsey}}}\cos(\Omega_{\text{Ramsey}}\tau)$ with fitting parameters $T_{\rm Ramsey}$ and $\Omega_{\rm Ramsey}$. Our result gives that $T_{\rm Ramsey} \sim$ 9.5 μ s and $\Omega_{Ramsey}/2\pi \sim 3.12$ MHz, which is consistent with $\Omega_{13}/2\pi = 3.11$ MHz obtained from Fig. 2A. Furthermore, we adjust the relative phase between the two $\pi/2$ pulses in the Ramsev sequence from $-\pi$ to π to change the rotation axis (33, 34). In Fig. 3C, the mixing current is plotted versus the angle of the rotation axis, $\Delta \varphi$, as well as the waiting time, and exhibits continuous variation of the excitation population in the A mode.

Rabi and Ramsey Oscillations at Different Coupling Strengths. The highly tunable coupling strength between resonators R_1 and R_3 offers promising prospect for phonon-state manipulation. We investigate the coherent dynamics under different coupling strength $\Omega_{13}/2\pi$, which can be tuned by varying the detuning between $R_1(R_3)$ and R_2 . Our results are presented in Fig. 4 A–C for Rabi oscillations and in Fig. 4 D–F for Ramsey interference. The oscillation frequencies $(\Omega_{\rm Rabi}/2\pi)$ and $\Omega_{\rm Ramsey}/2\pi$, respectively), and damping times $(T_{\rm Rabi})$ and $T_{\rm Ramsey}$, respectively) are extracted from the measured data. In Fig. 4 D and D, we plot the damping times as well as an effective quality factor, defined as the damping time multiplies

the corresponding oscillation frequency for the Rabi oscillations or the Ramsey interference. With our parameters, $\Omega_{\text{Rabi}}/2\pi$ remains almost the same (~0.25 MHz) for different coupling strength $\Omega_{13}/2\pi$, indicating that the coupling between the microwave burst to the mechanical resonators stays almost the same as the effective coupling varies. The Ramsey frequency $\Omega_{Ramsey}/2\pi$ remains consistent with $\Omega_{13}/2\pi$. Meanwhile, T_{Rabi} remains at ~11 μ s, and T_{Ramsey} varies from 5 to 10 µs, all having the same order of magnitude over a large range of effective coupling. Combining with the results shown in Fig. 2E, we can adjust oscillation frequencies $\Omega_{\text{Rabi}}/2\pi$ and $\Omega_{\text{Ramsey}}/2\pi$ by electrical tuning, which demonstrates tunable phonon dynamics in spatially separated graphene mechanical resonators. The coherent oscillation experiments were taken at driving power of \sim -45 dBm. Under this driving power, the relaxation rate of each mode is ~300 kHz, leading to the damping time in the coherent oscillation experiments $T_{\text{Rabi}} = T_{\text{Ramsey}} \sim 2/\gamma_i$ to be ~1 µs (SI Appendix, sections S7 and S8), which is comparable with T_{Rabi} and T_{Ramsey} obtained from the experiment.

Discussions

It is worth noting that at low driving power with a quality factor up to $\sim 10^5$, the zero-temperature cooperativity between the resonators can reach 10^7 . The measured damping times could be improved by optimizing the measurement setup to lower driving power to decrease the influence of nonlinear damping effects (25) in the future. Moreover, frequency stabilization such as feedback technique (35) can be utilized to suppress frequency fluctuations (28). Our results provide a promising platform for coherent computation using controllable vibrational phonons. Meanwhile, taking advantages of mechanical resonators being an outstanding interface between different physical systems, such as quantum dots engineered in graphene flakes (21), our architecture can be applied to transferring and storage of information between various systems. Although the present system is still a

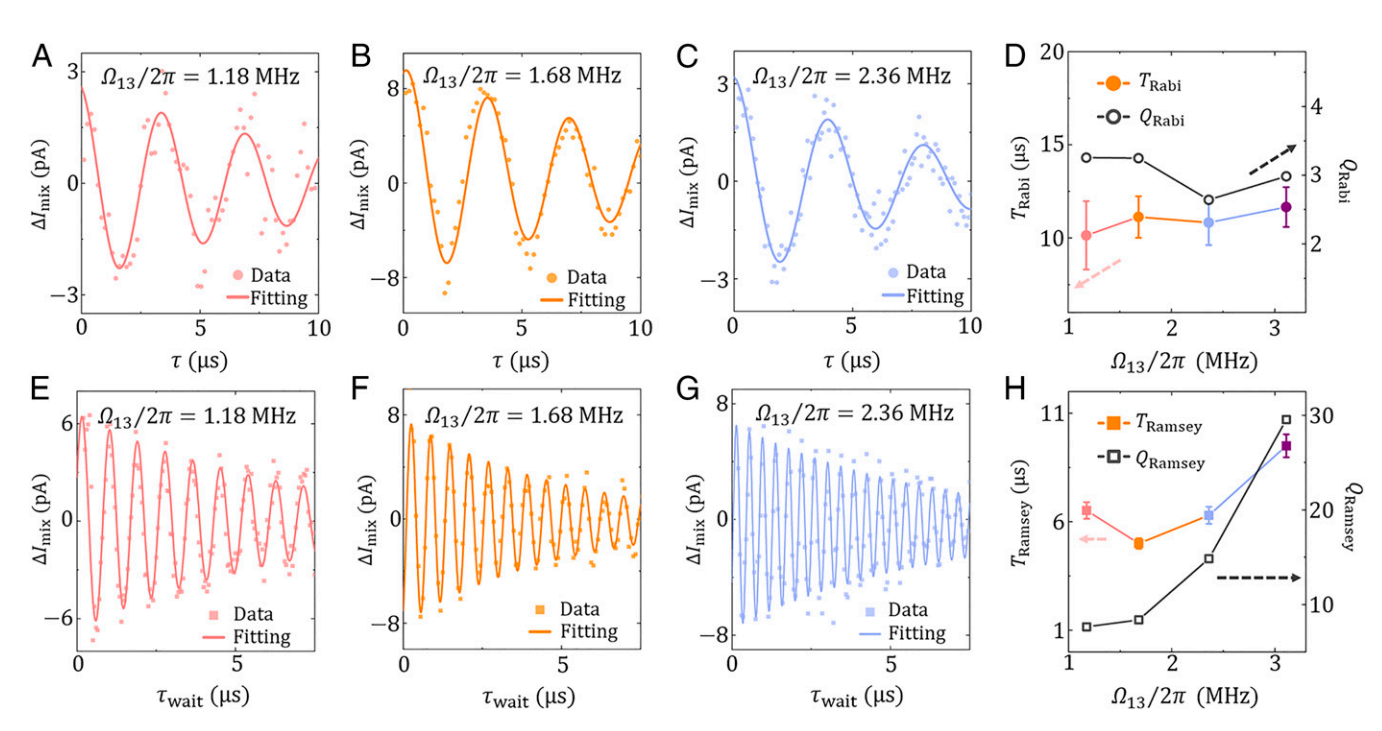


Fig. 4. Rabi and Ramsey oscillations at different coupling strengths. Phonon Rabi oscillations (A–C) and Ramsey interference (E–G) between spatially separated resonators at coupling strengths $\Omega_{13}/2\pi=1.18$, 1.68, and 2.36 MHz, respectively. Solid lines are numerical fitting using damped cosinusoidal functions. (D) Damping times of Rabi oscillations T_{Rabi} and quality factor $Q_{\text{Rabi}}=T_{\text{Rabi}}\times\Omega_{\text{Rabi}}/2\pi$ as functions of coupling rate $\Omega_{13}/2\pi$. (H) Damping times of Ramsey interference T_{Ramsey} and quality factor $T_{\text{Ramsey}} \times \Omega_{\text{Ramsey}} \times \Omega_{\text{Ramsey}}/2\pi$ as functions of coupling rate $\Omega_{13}/2\pi$. Error bars are given by fitting fidelities. Data points for $\Omega_{13}/2\pi=3.11$ MHz are taken from Figs. 2 and 3.

Zhang et al. PNAS Latest Articles | 5 of 6

classical one, the phonon occupation number at undriven state is ~2 [given by $\bar{n}_{th} = 1/(e^{\hbar\omega/k_BT} - 1) \sim 1.61$]. Using sideband cooling, advanced measurement setup, or resonators with higher frequency (36), our architecture can be pushed into quantum regime.

In conclusion, we studied coherent phonon dynamics between spatially separated graphene mechanical resonators. The giant cooperativity in our sample enables the study of such coherent oscillations and the fitting of the damping times. Our demonstration of coherent dynamics between mechanical modes with indirect interaction and high tunability is a key step toward on-demand state transfer and manipulation (6, 7, 33, 37) in an all-phonon platform. With the capabilities of system integrations, our architecture can be extended to large scale for phonon-based computing and longdistance information exchange in mechanical systems.

Materials and Methods

Sample Fabrication. A layer of SiN_x (50 nm) is deposited via low-pressure chemical vapor deposition on the silicon oxide layer, which covers a highly resistive silicon wafer. After electron beam lithography (EBL), three parallel trenches are etched through the SiNx layer by reactive ion etching, followed by dipping in buffered oxide etchant. The total etching depth is 200 nm. The widths of the trenches are designed as 2 µm. After a second EBL, 5 nm titanium and 20 nm gold are evaporated onto the wafer. All of the contacts are 1.5 μm in width. Finally, the graphene ribbon, exfoliated on a polydimethylsiloxane stamp, is aligned and transferred above the trenches (38).

Measurement Setup. For data acquisition in Figs. 1 D-F and 2A, an FM signal is generated by a Keysight E8257D microwave generator and applied to the

- 1. M. V. Gustafsson et al., Propagating phonons coupled to an artificial atom. Science 346, 207-211 (2014).
- 2. F. Lecocq, J. B. Clark, R. W. Simmonds, J. Aumentado, J. D. Teufel, Mechanically mediated microwave frequency conversion in the quantum regime, Phys. Rev. Lett. 116. 043601 (2016).
- 3. K. E. Khosla, M. R. Vanner, N. Ares, E. A. Laird, Displacemon electromechanics: How to detect quantum interference in a nanomechanical resonator. Phys. Rev. X 8, 021052 (2018)
- 4. C. F. Ockeloen-Korppi et al., Stabilized entanglement of massive mechanical oscillators. Nature 556, 478-482 (2018).
- 5. R. Riedinger et al., Remote quantum entanglement between two micromechanical oscillators. Nature 556, 473-477 (2018).
- 6. Y. Chu et al., Creation and control of multi-phonon Fock states in a bulk acousticwave resonator. Nature 563, 666-670 (2018).
- 7. K. J. Satzinger et al., Quantum control of surface acoustic-wave phonons. Nature 563,
- 8. L. D. Tóth, N. R. Bernier, A. Nunnenkamp, A. K. Feofanov, T. J. Kippenberg, A dissipative quantum reservoir for microwave light using a mechanical oscillator. Nat. Phys.
- 9. C. F. Ockeloen-Korppi et al., Low-noise amplification and frequency conversion with a multiport microwave optomechanical device, Phys. Rev. X 6, 041024 (2016).
- 10. T. Faust, J. Rieger, M. J. Seitner, J. P. Kotthaus, E. M. Weig, Coherent control of a classical nanomechanical two-level system. Nat. Phys. 9, 485-488 (2013).
- 11. D. Zhu et al., Coherent phonon Rabi oscillations with a high-frequency carbon nanotube phonon cavity. Nano Lett. 17, 915-921 (2017).
- 12. F. R. Braakman, N. Rossi, G. Tutuncuoglu, A. F. I. Morral, M. Poggio, Coherent twomode dynamics of a nanowire force sensor. Phys. Rev. Appl. 9, 054045 (2018).
- 13. H. Okamoto et al., Coherent phonon manipulation in coupled mechanical resonators. Nat. Phys. 9, 480-484 (2013).
- 14. G. Luo et al., Strong indirect coupling between graphene-based mechanical resonators via a phonon cavity. Nat. Commun. 9, 383 (2018).
- 15. K. Fang, M. H. Matheny, X. Luan, O. Painter, Optical transduction and routing of microwave phonons in cavity-optomechanical circuits. Nat. Photonics 10, 489-496
- 16. O. Di Stefano et al., Interaction of mechanical oscillators mediated by the exchange of virtual photon pairs. Phys. Rev. Lett. 122, 030402 (2019).
- C. Chen et al., Performance of monolayer graphene nanomechanical resonators with electrical readout. Nat. Nanotechnol. 4, 861-867 (2009).
- 18. R. De Alba et al., Tunable phonon-cavity coupling in graphene membranes. Nat. Nanotechnol. 11, 741-746 (2016).
- 19. J. P. Mathew, R. N. Patel, A. Borah, R. Vijay, M. M. Deshmukh, Dynamical strong coupling and parametric amplification of mechanical modes of graphene drums. Nat. Nanotechnol. 11, 747-751 (2016).

source of the center resonator R_2 , with deviation frequency $f_{\Delta} = 100$ kHz, modulation frequency $f_L = 1.33$ kHz; a Stanford Research SR830 lock-in amplifier is applied to read $I_{\rm mix}$ with frequency $f_{\rm L}$ at the drain of R_2 . For quality factor acquisition, $f_{\Delta}=1$ kHz, $f_{L}=233$ Hz. In Rabi and Ramsey oscillation experiments, the driving FM signal is constantly applied at the frequency of the lower state of the superposition state, i.e., eigenmode A in Fig. 2A. Additional driving pulse is generated by a Tektronix AWG7082C arbitrary waveform generator and applied to the gate electrode of R_1 . Here, the lock-in amplifier is set at a time constant of 300 ms with frequency f_L = 1.33 kHz. At each pulse parameter, $I_{\rm mix}$ is acquired for over 40 times. The repetition rate of the waveform is 20 \sim 50 kHz in different experiments. Hence the total average times is over $2.4 \times 10^5 \sim 6 \times 10^5$. Here, the measured I_{mix} , which is averaged over many pulse cycles, can be recognized as the occupation of eigenmode A.

Data Availability. All data supporting the findings of this study are available within the article and/or the SI Appendix, with corresponding raw data deposited at Zenodo (39).

ACKNOWLEDGMENTS. The authors would like to thank J. Moser for fruitful discussions in sample fabrication and measurement techniques. This work was supported by the National Key Research and Development Program of China (Grant 2016YFA0301700), the National Natural Science Foundation of China (Grants 11625419, 61704164, 61674132, 11674300, 11575172, 61904171, and 11904351), China Postdoctoral Science Foundation (Grants BX20180295 and 2018M640586), and the Anhui Initiative in Quantum Information Technologies (Grant AHY080000). L.T. is supported by the National Science Foundation under Award PHY-1720501, and the University of California Multicampus-National Lab Collaborative Research and Training under Award LFR-17-477237. This work was partially carried out at the University of Science and Technology of China Center for Micro and Nanoscale Research and Fabrication.

- 20. J. Güttinger et al., Energy-dependent path of dissipation in nanomechanical resonators. Nat. Nanotechnol. 12, 631-636 (2017).
- 21. G. Luo et al., Coupling graphene nanomechanical motion to a single-electron transistor Nanoscale 9 5608-5614 (2017)
- 22. L. Novotny, Strong coupling, energy splitting, and level crossings: A classical perspective. Am. J. Phys. 78, 1199-1202 (2010).
- 23. M. Frimmer, L. Novotny, The classical Bloch equations. Am. J. Phys. 82, 947–954 (2014).
- 24. V. Gouttenoire et al., Digital and FM demodulation of a doubly clamped singlewalled carbon-nanotube oscillator: Towards a nanotube cell phone. Small 6, 1060-1065 (2010)
- 25. J. Moser, A. Eichler, J. Güttinger, M. I. Dykman, A. Bachtold, Nanotube mechanical resonators with quality factors of up to 5 million. Nat. Nanotechnol. 9, 1007-1011
- 26. A. Eichler et al., Nonlinear damping in mechanical resonators made from carbon nanotubes and graphene. Nat. Nanotechnol. 6, 339-342 (2011).
- 27. S. Manzeli, D. Dumcenco, G. Migliato Marega, A. Kis, Self-sensing, tunable monolayer MoS₂ nanoelectromechanical resonators. Nat. Commun. 10, 4831 (2019).
- 28. M. Sansa et al., Frequency fluctuations in silicon nanoresonators. Nat. Nanotechnol. 11, 552-558 (2016).
- 29. A. Eichler, M. del Álamo Ruiz, J. A. Plaza, A. Bachtold, Strong coupling between mechanical modes in a nanotube resonator. Phys. Rev. Lett. 109, 025503 (2012).
- 30. C. H. Liu, I. S. Kim, L. J. Lauhon, Optical control of mechanical mode-coupling within a MoS₂ resonator in the strong-coupling regime. Nano Lett. 15, 6727-6731 (2015).
- 31. S. X. Li et al., Parametric strong mode-coupling in carbon nanotube mechanical resonators. Nanoscale 8, 14809-14813 (2016).
- 32. M. O. Scully, M. S. Zubairy, Quantum Optics (Cambridge University Press, Cambridge, ed. 1, 1997), p. 652.
- 33. D. Kim et al., Microwave-driven coherent operation of a semiconductor quantum dot charge qubit. Nat. Nanotechnol. 10, 243-247 (2015).
- 34. L. M. K. Vandersypen, I. L. Chuang, NMR techniques for quantum control and computation. Rev. Mod. Phys. 76, 1037-1069 (2004).
- 35. Y. Wen et al., A coherent nanomechanical oscillator driven by single-electron tunnelling. Nat. Phys. 16, 75-82 (2020).
- 36. A. D. O'Connell et al., Quantum ground state and single-phonon control of a mechanical resonator. Nature 464, 697-703 (2010).
- 37. D. Vion et al., Manipulating the quantum state of an electrical circuit. Science 296, 886-889 (2002)
- 38. A. Castellanos-Gomez et al., Deterministic transfer of two-dimensional materials by all-dry viscoelastic stamping. 2D Mater. 1, 011002 (2014).
- 39. Z.-Z. Zhang et al., Data from "Coherent phonon dynamics in spatially separated graphene mechanical resonators." Zenodo. https://zenodo.org/record/3594242#. XkXKiGhKhPY. Deposited 29 December 2019.